Electronic Supplementary Information (ESI)

Anionic Exchange Membrane Water Electrolysis over Superparamagnetic Ferrites

*Tiago Fernandes,[a] Ramsundar Mohan,[a] Laura Donk,[b] Wei Chen,[b] Chiara Biz,[c] Mauro Fianchini,[c,d] Saeed Kamali,[e,f] Siavash Mohammad Alizadeh,[a] Anna Kitayev,[g] Aviv Ashdot,[g] Miles Page,[g] Laura M. Salonen,[i,a] Sebastian Kopp,[h] Ervin Tal Gutelmacher,[g] José Gracia,[c] Marta Costa Figueiredo,[b] and Yury V. Kolen'ko[a,]**

[a] International Iberian Nanotechnology Laboratory, Braga 4715-330, Portugal

[b] Department of Chemical Engineering and Chemistry, Eindhoven University of Technology, Eindhoven 5600 MB, Netherlands

[c] MagnetoCat SL, Calle General Polavieja 9, 3Izq, Alicante 03012, Spain

[d] Departamento de Química Física, Universidad de Alicante, Carretera San Vicente del Raspeig s/n, 03690 San Vicente del Raspeig, E-03080 Alicante, Spain

[e] Department of Physics and Astronomy, Middle Tennessee State University, Murfreesboro, TN, United States

[f] Department of Mechanical, Aerospace and Biomedical Engineering, University of Tennessee Space Institute, Tullahoma, TN, United States

[g] HYDROLITE, Hatohen 2, Caesarea 3088900, Israel

[h] Hydrogen Technologies, Fraunhofer Institute for Solar Energy Systems ISE, Freiburg 79110, Germany

[i] CINBIO, Universidade de Vigo, Department of Organic Chemistry, 36310 Vigo, Spain

* yury.kolenko@inl.int

TABLES

Table S1. Average particle diameters, calculated lattice parameters, specific surface area and optical bandgap of the $CoFe_2O_4$, $NiFe_2O_4$, $ZnFe_2O_4$, and $Zn_{0.2}Mn_{0.2}Ni_{0.2}Co_{0.2}Fe_{2.2}O_4$ ($4A_{1/4}Fe_{2.2}O_4$) catalysts synthesized by coprecipitation method followed by calcination and ball milling.

Sample	Mean crystallite size* (nm)	Calculated lattice parameters ($a = b = c$) (Å)*	Mean particle radius (nm)**	Specific surface area S_{BET} (m^2/g)***	Optical bandgap (eV)
$CoFe_2O_4$	34.0^{+} $32.1^{\bullet}$	8.3416 $8.3432^{\bullet}$	20 ± 7	65	1.48
$NiFe_2O_4$	24.9^{+} $28.2^{\bullet}$	8.3445 $8.3461^{\bullet}$	26 ± 6	42	1.58
$ZnFe_2O_4$	20.9^{+} $23.8^{\bullet}$	8.4437 $8.4629^{\bullet}$	18 ± 4	54	1.70
$4A_{1/4}Fe_{2.2}O_4$	25.9^{+}	8.3832	21 ± 5	84	1.51

* Calculated from the collected XRD data ($^{+}$Scherrer Equation/•Rietveld Refinement).

** Estimated by the analysis of TEM images (Figure S3).

*** Estimated by N_2 physisorption.

Table S2. Summary of the refined Mössbauer parameters (centroid shift, δ, quadrupole shift, ε, magnetic hyperfine field, B_{hf}, magnetic hyperfine field distribution, σ, intensity, I) for spectra collected at 6 K from $CoFe_2O_4$, $NiFe_2O_4$, $ZnFe_2O_4$, and $Zn_{0.2}Mn_{0.2}Ni_{0.2}Co_{0.2}Fe_{2.2}O_4$ catalysts synthesized by coprecipitation method followed by calcination and ball milling. Estimated errors are ± 3% in I, ± 0.005 mm/s in δ and ε, and ± 0.2 T in B_{hf} and σ.

	Parameters	**$CoFe_2O_4$**	**$NiFe_2O_4$**	**$ZnFe_2O_4$**	**$Zn_{0.2}Mn_{0.2}Ni_{0.2}Co_{0.2}Fe_{2.2}O_4$**
	δ_1 (mm/s)	0.524	0.468	0.452	0.627
	B_{hf1} (T)	52.2	54.9	50.9	52.3
***Q*₁**	σ_1 (T)	1.8	0.7	1.2	1.0
	ε_1 (mm/s)	0.007	–0.004	0.069	0.042
	I_1 (%)	46	46	48	23
	δ_2 (mm/s)	0.328	0.361	0.442	0.337
	B_{hf2} (T)	50.7	50.7	50.1	51.5
***Q*₂**	σ_2 (T)	1.2	0.8	1.2	1.0
	ε_2 (mm/s)	0.004	0.052	–0.127	–0.003
	I_2 (%)	32	39	32	45
	δ_3 (mm/s)	0.428	0.367	0.452	0.447
	B_{hf3} (T)	48.7	50.2	46.3	49.8
***Q*₃**	σ_3 (T)	3.3	0.7	3.6	2.8
	ε_3 (mm/s)	–0.026	–0.138	–0.006	–0.030
	I_3 (%)	22	15	20	32
	Absorption (%)	8.0	7.3	6.9	7.4

Table S3. Cation distributions within the spinel crystal structure estimated based on the 6 K Mössbauer data collected from the $CoFe_2O_4$, $NiFe_2O_4$, $ZnFe_2O_4$, and $Zn_{0.2}Mn_{0.2}Ni_{0.2}Co_{0.2}Fe_{2.2}O_4$ catalysts synthesized by coprecipitation method followed by calcination and ball milling. *A* = tetrahedral sites, B = octahedral sites of the AB_2O_4 spinel structure.

Compound	Distributions
$CoFe_2O_4$	$[Co_{0.36}Fe_{0.64}]^A\{Co_{0.64}Fe_{1.36}\}^BO_4$
$NiFe_2O_4$	$[Fe]^A\{NiFe\}^BO_4$
$ZnFe_2O_4$	$[Zn_{0.36}Fe_{0.64}]^A\{Zn_{0.64}Fe_{1.36}\}^BO_4$
$Zn_{0.2}Mn_{0.2}Ni_{0.2}Co_{0.2}Fe_{2.2}O_4$	$[M_{0.10}Fe_{0.90}]^A\{M_{0.90}Fe_{1.10}\}^BO_4$

Table S4. Magnetic properties of the $CoFe_2O_4$, $NiFe_2O_4$, $ZnFe_2O_4$, and $Zn_{0.2}Mn_{0.2}Ni_{0.2}Co_{0.2}Fe_{2.2}O_4$ catalysts synthesized by coprecipitation method followed by calcination and ball milling.

Catalyst	M_s (emu/g_{sample})	M_r (emu/g_{sample})	Hc (Oe)
$CoFe_2O_4$	38.5	15.9	600
$NiFe_2O_4$	44.2	5.7	72
$ZnFe_2O_4$	15.0	0.0	0
$Zn_{0.2}Mn_{0.2}Ni_{0.2}Co_{0.2}Fe_{2.2}O_4$	50.3	3.7	40

Table S5. ICP-OES analysis of detailing elemental composition of the catalysts explored in this work.

Element	Experimental Mole Fraction to Fe	Theoretical Mole Fraction to Fe	% diff.
Co ($CoFe_2O_4$)	2.00	2.00	0.00
Ni ($NiFe_2O_4$)	1.99	2.00	-0.08
Zn ($ZnFe_2O_4$)	2.04	2.00	+2.39
$Zn_{0.2}Mn_{0.2}Ni_{0.2}Co_{0.2}Fe_{2.2}O_4$			
Zn	0.095	0.091	+4.29
Mn	0.103	0.091	+13.66
Ni	0.100	0.091	+10.27
Co	0.099	0.091	+9.74

Table S6. Comparison of alkaline OER activity for several reported simple, as well as high-entropy spinels and metal oxides.

Catalyst	Support	Overpotential η_{10} @ 10mA/cm^2	Tafel slope (mV/dec)	Electrolyte	Ref.
H_2-treated $NiFe_2O_4$	Glassy carbon	389 mV	64	1 M KOH	[1]
$CoFe_2O_4$ with carbon spheres	Glassy carbon	390 mV	58	1 M KOH	[2]
Dual-phase $MnCo_2O_4$	Glassy carbon	327 mV	79	1 M KOH	[3]
Mesoporous $NiFe_2O_4$ nanorods	Glassy carbon	342 mV	44	1 M KOH	[4]
Mesoporous $NiFe_2O_4$	Glassy carbon	410 mV	50	1 M KOH	[5]
$ZnFe_2O_4$ NPs on N-doped graphene	Nickel foam	240 mV	64	1 M KOH	[6]
$MnFe_2O_4$	Glassy carbon	600 mV	116	0.1 M KOH	[7]
$CuFe_2O_4$, $NiFe_2O_4$, $CoFe_2O_4$	Nickel foam	369 mV ($CuFe_2O_4$) 386 mV ($NiFe_2O_4$) 448 mV ($CoFe_2O_4$)	76 ($CuFe_2O_4$) 86 ($NiFe_2O_4$) 148 ($CoFe_2O_4$)	1 M KOH	[8]
Mesoporous nanostructured AFe_2O_4 (A = Co, Mn, Ni)	Glassy carbon	412 mV ($CoFe_2O_4$) 412 mV ($NiFe_2O_4$) 582 mV ($MnFe_2O_4$)	–	0.1 M KOH	[9]
$CoFe_2O_4$ nanocubes on a N-doped graphene oxide	Glassy carbon	320 mV	56	1 M KOH	[10]
$Co_{0.8}Zn_{0.2}Fe_2O_4$	Ni foam	317 mV	43	1 M KOH	[11]
$Ni_{0.5}Cu_{0.5}Fe_2O_4$ anchored at S-doped g-C_3N_4	316 SSL mesh	250 mV	45	1 M KOH	[12]
$Co_{0.5}Ni_{0.5}Fe_2O_4$	Ni foam	210 mV	35	1 M KOH	[13]
$(NiCoMnCu)_1Fe_1Co_1O_4$	Carbon paper	460 mV	–	1 M KOH	[14]
$(CoFeNiCrMn)_3O_4$	FTO	307 mV	30	1 M KOH	[15]
$(Co_{0.2}Mn_{0.2}Ni_{0.2}Fe_{0.2}Zn_{0.2})Fe_2O_4$	CFP	326 mV	54	1 M KOH	[16]
$(CoNiMnZnFe)_3O_{3.2}$	CFP	336 mV	48	1 M KOH	[17]
$CoFe_2O_4$	Glassy carbon	484 mV	103	1 M KOH	This work
$NiFe_2O_4$	Glassy carbon	455 mV	108	1 M KOH	This work
$Zn_{0.2}Mn_{0.2}Ni_{0.2}Co_{0.2}Fe_{2.2}O_4$	Glassy carbon	432 mV	86	1 M KOH	This work

Table S7. Comparison of full-cell AEMEL performance of several spinels reported to date.

Anode material	Membrane/ Supporting electrolyte	Loading Cell size	Performance @ ~2V	Electrolyte	Stability test	Ref
$NiFe_2O_4$	Fumasep® FAA3-50	3 mg/cm^2 5 cm^2	2.7 A/cm^2 60 °C	1 M KOH	70 h	[18]
$NiFeO_x$	SustainionTM X37-50	2.5 mg/cm^2 5 cm^2	0.650 A/cm^2 50 °C	1 M KOH	500 h	[19]
$NiFe_2O_4$	Fumasep® FAA3-50	3 mg/cm^2 5 cm^2	2.5 A/cm^2 60 °C	1 M KOH	100 h	[20]
$NiMn_2O_4$	Fumasep® FAA3-50	3 mg/cm^2 5 cm^2	0.530 A/cm^2 80 °C	1 M KOH	1000 h	[21]
$Ce_{0.2}MnFe_{1.8}O_4$	Fumasep® FAA-3-PK-130	3.5 mg/cm^2 4 cm^2	0.300 A/cm^2 (@ 1.8 V) 25 °C	1 M KOH	100 h	[22]
$Ni_{0.75}Fe_{2.25}O_4$	X37-50 Grade T	4 mg/cm^2 7.1 cm^2	2.5 A/cm^2 (@1.9V) 45 °C	1 M KOH	21 h	[23]
NiFe-oxide	Fumasep® FAA3-50	5 cm^2	3.25 A/cm^2 at 2.2 V 60°C	1 M KOH	100 h	[24]
$NiCo_2O_4$/CNF	Fumasep® FAA3-50	3 mg/cm^2	0.303 A/cm^2 at 1.8 V 50°C	6 M KOH	-	[25]
$Ni_{0.6}Co_{0.2}Fe_{0.2}$	Fumapem-3-PE-30	5 mg/cm^2 25 cm^2	2 A/cm^2 50 °C	1 M KOH	50 h	[26]
$Zn_{0.2}Mn_{0.2}Ni_{0.2}Co_{0.2}Fe_{2.2}O_4$	Proprietary Hydrolite Membrane B 70 µm	3 mg/cm^2 4 cm^2	**1.5 A/cm^2 80 °C**	1 M KOH	20 h	This work
$NiFe_2O_4$	Proprietary Hydrolite Membrane B 70 µm	3 mg/cm^2 4 cm^2	**1.9 A/cm^2 80 °C**	1 M KOH	20 h	This work

FIGURES

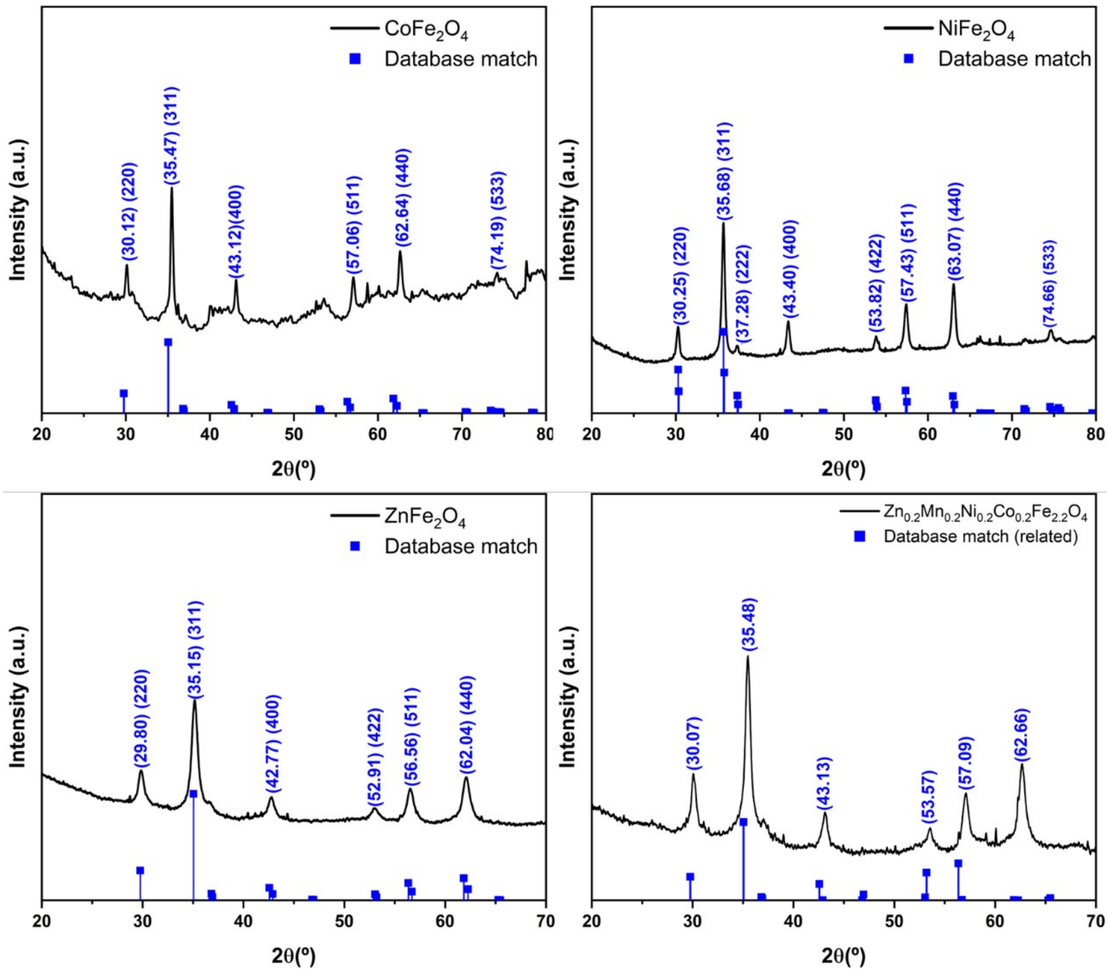

Figure S1. XRD patterns for $CoFe_2O_4$ (ICDD no. 01-090-3471, cubic, *Fd*-3*m*), $NiFe_2O_4$ (ICDD no. 01-078-3741, cubic, *Fd*-3*m*), $ZnFe_2O_4$ (ICDD no. 04-008-5691, cubic, *Fd*-3*m*), and $Zn_{0.2}Mn_{0.2}Ni_{0.2}Co_{0.2}Fe_{2.2}O_4$ catalysts synthesized by coprecipitation method followed by calcination and ball milling.

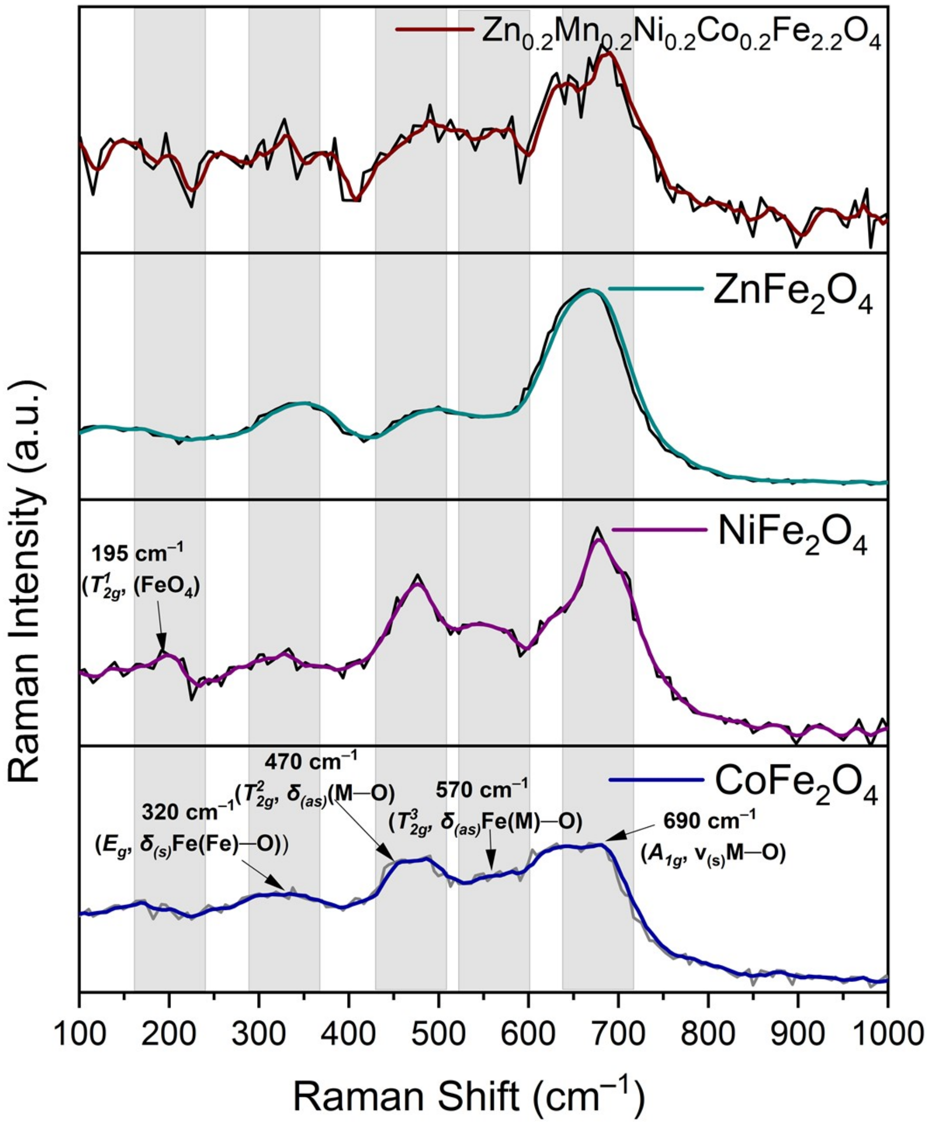

Figure S2. Room temperature Raman spectra for $CoFe_2O_4$, $NiFe_2O_4$, $ZnFe_2O_4$, and $Zn_{0.2}Mn_{0.2}Ni_{0.2}Co_{0.2}Fe_{2.2}O_4$ catalysts synthesized by coprecipitation method followed by calcination and ball milling.

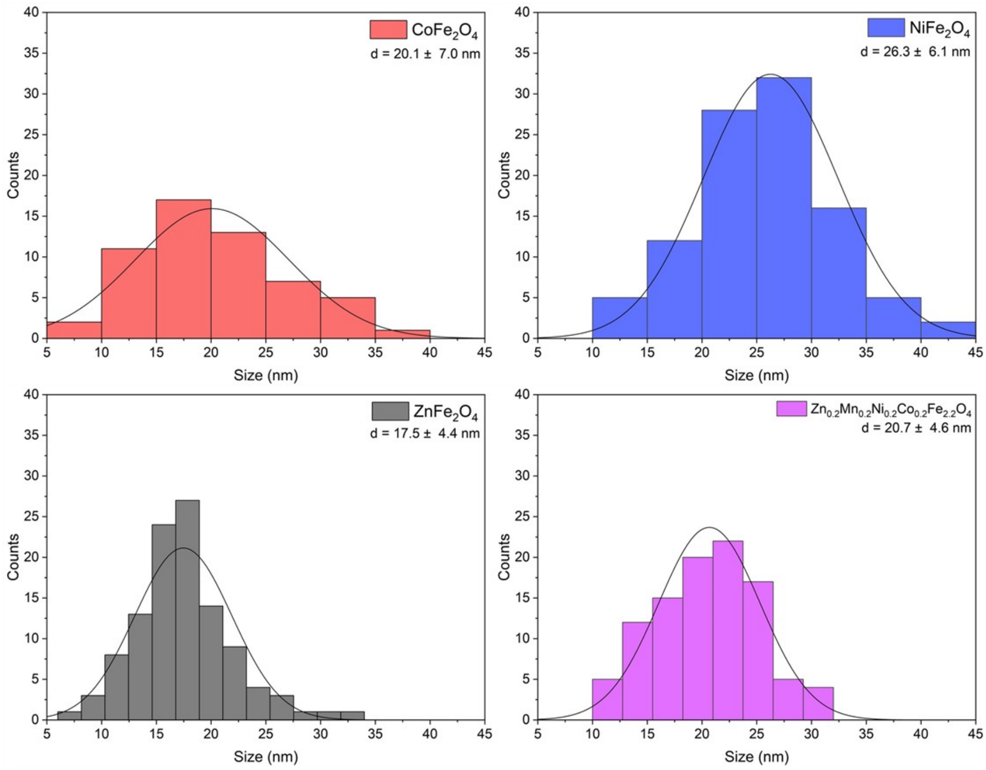

Figure S3. Histograms of particle-size distribution as determined from several TEM images of $CoFe_2O_4$, $NiFe_2O_4$, $ZnFe_2O_4$, and $Zn_{0.2}Mn_{0.2}Ni_{0.2}Co_{0.2}Fe_{2.2}O_4$ catalysts synthesized by coprecipitation method followed by calcination and ball milling, n = 100. The curve shows a fit using the Gaussian distribution function. The mean particle size is indicated in the respective plot where the error is the standard deviation.

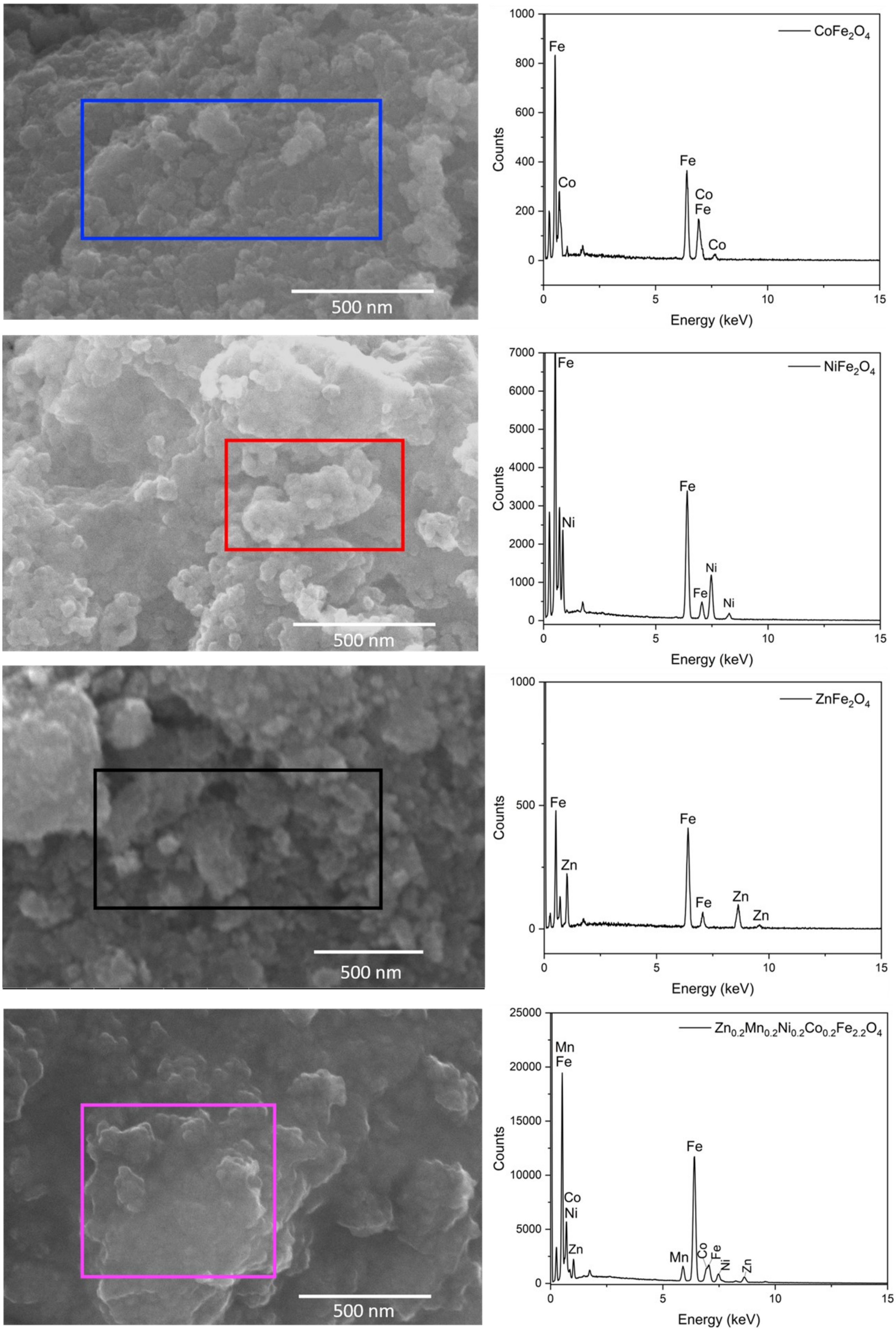

Figure S4. Representative SEM and SEM−EDX data of $CoFe_2O_4$, $NiFe_2O_4$, $ZnFe_2O_4$, and $Zn_{0.2}Mn_{0.2}Ni_{0.2}Co_{0.2}Fe_{2.2}O_4$ catalysts synthesized by coprecipitation method followed by calcination and ball milling.

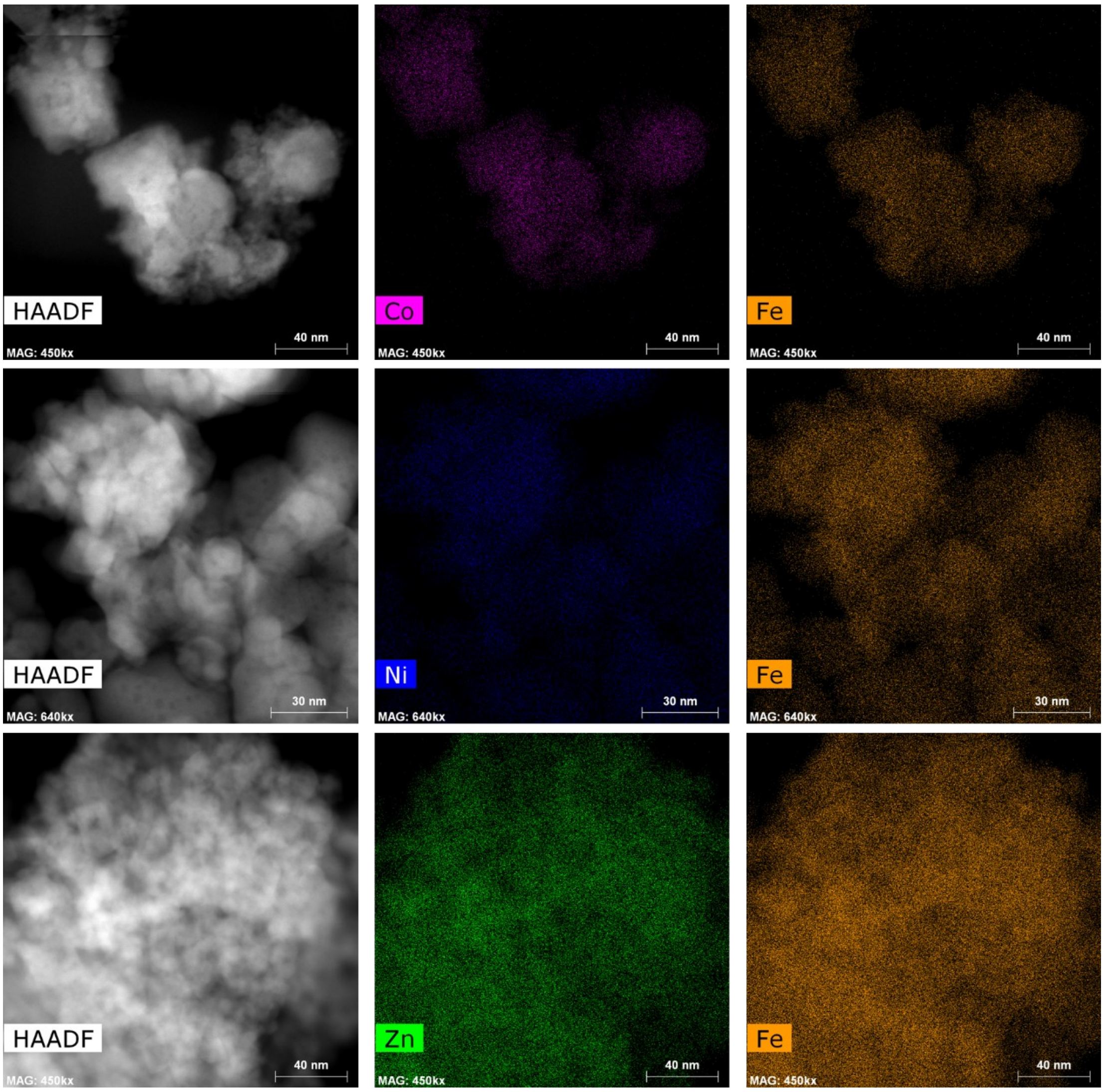

Figure S5. HAADF−STEM image and the corresponding EDX elemental mapping of $CoFe_2O_4$ (top), $NiFe_2O_4$ (middle), and $ZnFe_2O_4$ (bottom) catalysts.

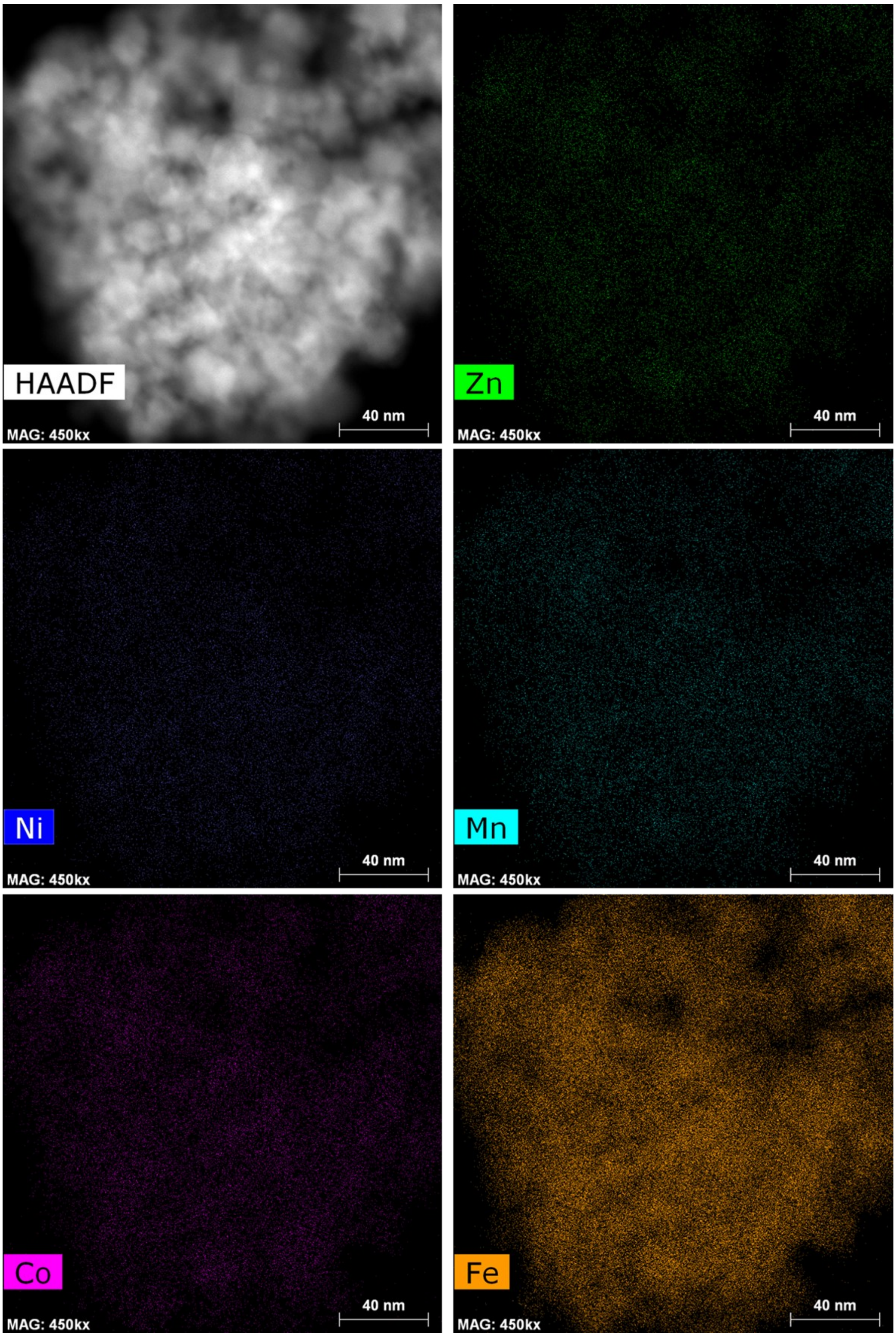

Figure S6. HAADF−STEM image and the corresponding EDX elemental mapping of the compositionally complex $Zn_{0.2}Mn_{0.2}Ni_{0.2}Co_{0.2}Fe_{2.2}O_4$ ferrite catalyst.

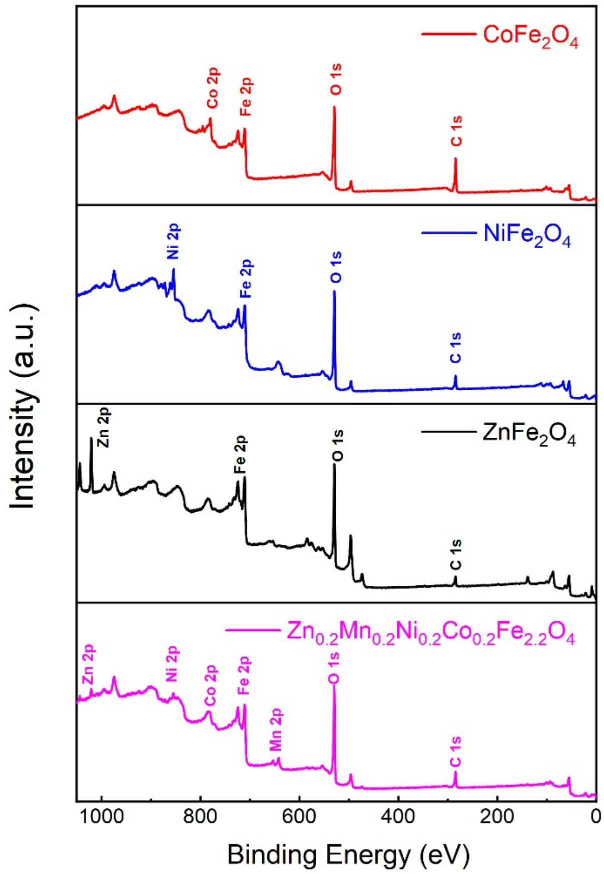

Figure S7. XPS survey data for the key constituting elements of $CoFe_2O_4$, $NiFe_2O_4$, $ZnFe_2O_4$, and $Zn_{0.2}Mn_{0.2}Ni_{0.2}Co_{0.2}Fe_{2.2}O_4$ catalysts synthesized by coprecipitation method followed by calcination and ball milling.

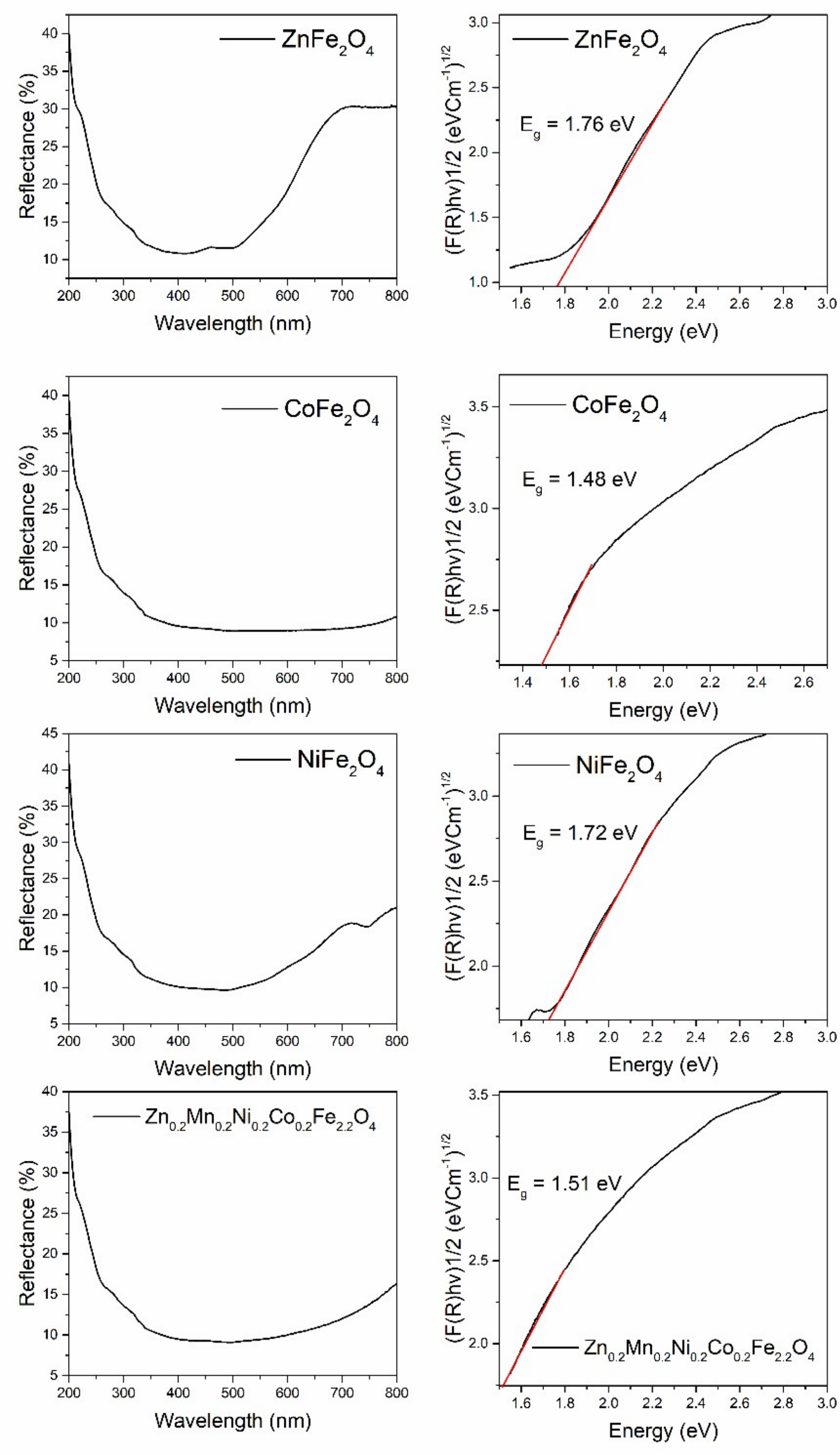

Figure S8. UV/Vis diffuse reflectance spectra of $CoFe_2O_4$, $NiFe_2O_4$, $ZnFe_2O_4$, and $Zn_{0.2}Mn_{0.2}Ni_{0.2}Co_{0.2}Fe_{2.2}O_4$ catalysts synthesized by coprecipitation method followed by calcination and ball milling, together with the corresponding Tauc plots (inset) used for the determination of the optical band gap.

COMPUTATIONAL STUDY ON SPINEL FERRITES

Computational method

The study was performed by periodic DFT calculations using QUANTUM ESPRESSO 6.8 (QE) GPU-enabled version.[27] The DFT+U+J approach[28] was applied to account for the strong correlation among the electrons in the *3d*-metals (U = 2.5 eV, J = 0.4 eV, U_{eff} = 2.5 eV) during the geometry optimization of the lattice parameters (atomic positions + cell). U_{eff} follows the Dudarev *et al* formulation[28c]. All the calculations were carried out with spin polarization and by applying the collinear magnetic model (i.e., all atomic magnetic moments are aligned with the z-axis), unless specified. The exchange−correlation energy was calculated within the generalized gradient approximation using the optB86b functional.[29] The electron−ion interactions for the atoms were described by the Ultrasoft (US) method developed by Vanderbilt.[30] The US pseudopotentials used in this work were generated by using the atomic package *ld1.x* included in the Quantum ESPRESSO distribution (https://www.quantum-espresso.org/documentation/package-specific-documentation/). The pseudopotentials were recompiled for optB86b from Andrea Dal Corso's schemes (proposed for PBE and PBEsol) in pslibrary[31] (https://github.com/dalcorso/pslibrary.git). The kinetic energy cut-offs used in optimization were set to 60 Ry for wavefunction and 600 Ry for charge density and potential. A single point energy refinement of optimized structures was carried out for each of the most stable entries. The Monkhorst−Pack scheme was chosen for the integration in the reciprocal space.[32] The reciprocal space of all investigated structures was generally sampled with a 0.20 $Å^{-1}$-spaced k-points grid for optimizations and energy refinements. The projectors for U on localized orbitals were based on Löwdin orthogonalized atomic wavefunctions orbitals ("ortho-atomic" option in QE). Marzari−Vanderbilt−Devita−Payne smearing[33] was used for all the calculations. The computational studies presented in this article are carried out at 0 K and under vacuum condition.

Computational remarks

The computational models were built based on the cation distribution data obtained from Mössbauer spectroscopy (see Table S3). The space groups are reported in Hermann−Mauguin symmetry symbols. CS and C indicate the Crystallographic System and the cubic symmetry, respectively. The cell parameters are indicated as a;b;c (in Å), α;β;γ (in º) and the cell volume is in Å. Average M−O bond distances are reported in Å, where M is the *3d*-transition metal in the octahedral (O_h) or tetrahedral (T_d) site. Magnetic orderings are labelled as: FM (ferromagnetic), AFM (antiferromagnetic), ferri (ferrimagnetic), NM (non-magnetic, non-spin-polarized calculation), while the types of conduction are indicated as M (metallic), HM (half metallic), S (semiconduction) and I (insulator). For all entries only the spin components of the magnetic moments (μ, in μ_B) are reported.[34]

Pictures and surfaces are created using VESTA[35] program. Mn, Fe, Co, Ni, Zn, and O are colored in pink, brown, blue, silver, dark grey, and red, respectively. The isosurfaces in the density spin plots are shown at 0.004 a_0^{-3}(a_0 is the Bohr radius). Density of states (DOS) are generated with Gnuplot v. 5.4[36] (http://www.gnuplot.info/).

Computational data tables

$CoFe_2O_4$ ($[Co_{0.375}Fe_{0.625}]^{A}\{Co_{0.625}Fe_{1.375}\}^{B}O_4$)

Table S8. Optimized computational data on partially inverse $CoFe_2O_4$ bulk (T = 0 K). The most stable ground state is referred to as 0.00 eV. The experimental lattice parameters are $a = b = c$ = 8.3416 Å, as reported in Table S1.

CS (C)	Magn. Struc. type	Δ*E* (eV)	Cell parameters (Å)	Cell volume (Å^3)	Average M–O distance (Å)	Abs. Average Mag. Mom. (|μ_B|)
Fd-3m	NM	37.01	a=8.06291; b=7.69179; c=8.08933; α=89.82°; β=90.64°; γ=89.93°	501.65	1.83 (Fe-O T_d) 1.92 (Fe-O O_h) 1.88 (Co-O T_d) 1.91 (Co-O O_h)	-
	FM	No convergence				
	Ferri1	**0.00**	**a=8.40838; b=8.37131; c=8.36615; α=90.39°; β=89.85°; γ=90.00°**	**588.87**	**1.89 (Fe-O T_d) 2.03 (Fe-O O_h) 1.95 (Co-O T_d) 2.06 (Co-O O_h)**	**4.0 (Fe) 2.5 (Co)**
	Ferri2	2.98	a=8.42534; b=8.44037; c=8.42766; α=90.06°; β=89.92°; γ=89.93°	599.32	1.91 (Fe-O T_d) 2.03 (Fe-O O_h) 1.96 (Co-O T_d) 2.07 (Co-O O_h)	4.1 (Fe) 2.5 (Co)

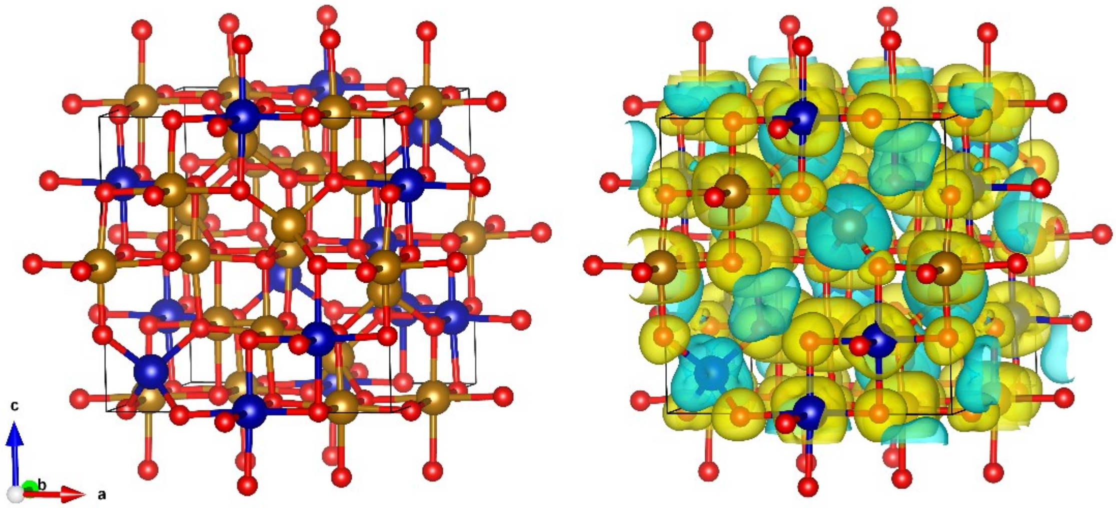

Figure S9. Optimized cell (right) and spin density plot (left) of ferrimagnetic (Ferri 1) bulk $CoFe_2O_4$ partially inverse spinel (yellow = spin up, cyan = spin down).

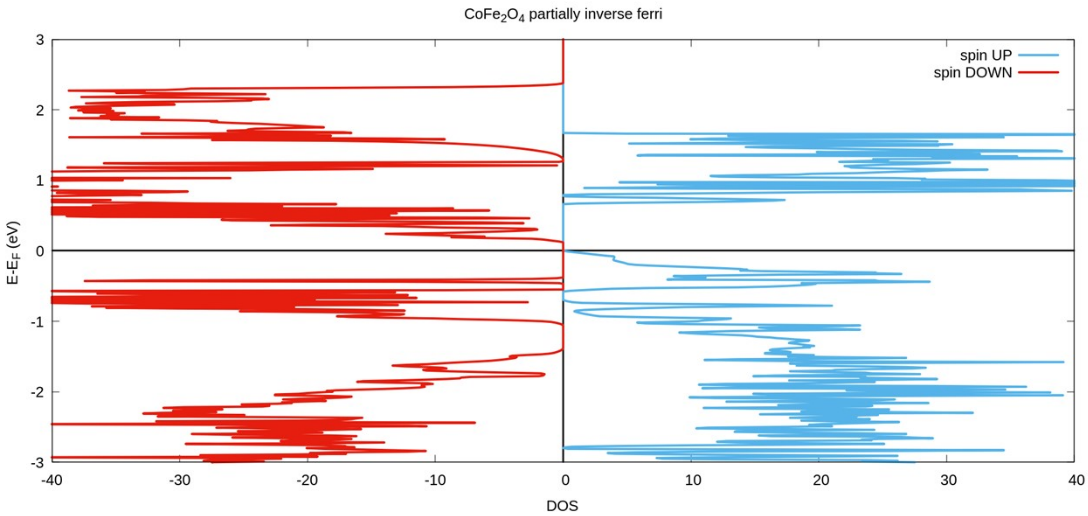

Figure S10. Density of states (DOS) between −3 eV and 3 eV of ferrimagnetic (Ferri 1) bulk $CoFe_2O_4$ partially inverse spinel.

$NiFe_2O_4$ ($[Fe]^A\{NiFe\}^BO_4$)

Table S9. Optimized computational data on <u>inverse spinel</u> $NiFe_2O_4$ bulk ($T = 0$ K). The most stable ground state is referred to as 0.00 eV. The experimental lattice parameters are $a = b = c = 8.3445$ Å, as reported in Table S1.

CS (C)	Magn. Struc. type	Δ*E* (eV)	Cell parameters (Å)	Cell volume (Å^3)	Average M–O distance (Å)	Abs. Average Mag. Mom. (|μ_B|)
Fd-3m	NM	39.70	a=8.06116; b=7.81116; c=8.08496; α=89.70º; β=90.15; γ=89.89º	509.08	1.81 (Fe-O T_d) 1.93 (Fe-O O_h) 1.96 (Ni-O O_h)	-
	FM	No convergence				
	AFM	1.17	a=8.34447; b=8.32816; c=8.35281; α=90.36º; β=90.15º; γ=90.46º	580.44	1.90 (Fe-O T_d) 2.02 (Fe-O O_h) 2.05 (Ni-O O_h)	4.0 (Fe) 1.6 (Ni)
	Ferri	**0.00**	**a=8.33734; b=8.30763; c=8.34308; α=90.00º; β=90.08º; γ=90.06º**	**577.87**	**1.89 (Fe-O T_d) 2.02 (Fe-O O_h) 2.04 (Ni-O O_h)**	**4.0 (Fe) 1.5 (Ni)**

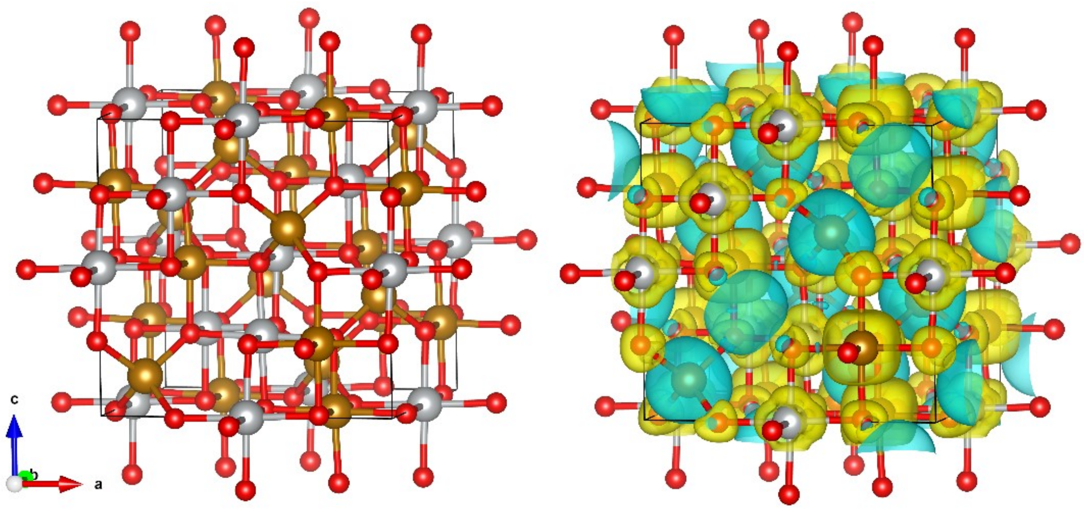

Figure S11. Optimized cell (right) and spin density plot (left) of ferrimagnetic bulk $NiFe_2O_4$ inverse spinel (yellow = spin up, cyan = spin down).

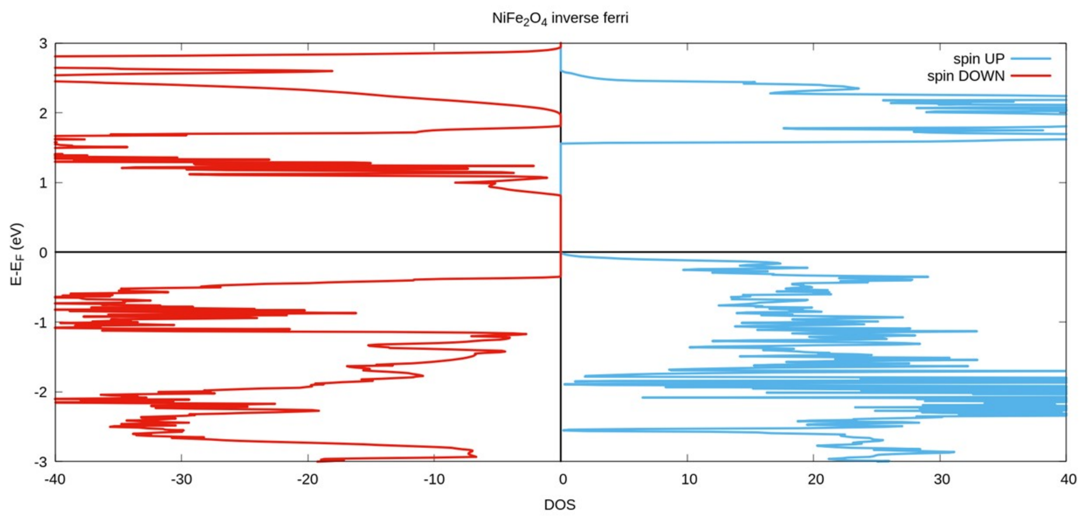

Figure S12. Density of states (DOS) between −3 eV and 3 eV of ferrimagnetic bulk $NiFe_2O_4$ inverse spinel.

$NiFe_{2-x}O_4$ (x = 0.125) **($[Fe]^{A}\{NiFe_{0.875}\}^{B}O_4$)**

Table S10. Optimized computational data on <u>inverse spinel</u> $NiFe_{2-x}O_4$ (x = 0.125) bulk (T = 0 K). The most stable ground state is referred to as 0.00 eV. The experimental lattice parameters are $a = b = c$ = 8.3445 Å, as reported in Table S1.

CS (C)	**Magn. Struc. type**	**Δ*E* (eV)**	**Cell parameters (Å)**	**Cell volume (Å³)**	**Average M–O distance (Å)**	**Abs. Average Mag. Mom. (|μ_B|)**
Fd-3m	NM	34.54	a=8.03199; b=7.80771; c=8.06645; α=90.06º; β=90.50º; γ=89.80º	505.84	1.80 (Fe-O T_d) 1.91 (Fe-O O_h) 1.97 (Ni-O O_h)	-
	FM	No convergence				
	Ferri	**0.00**	**a=8.24776; b=8.33943; c=8.30065; α=89.82º; β=89.91º; γ=90.33º**	**570.92**	**1.88 (Fe-O T_d) 2.05 (Fe-O O_h) 1.99 (Ni-O O_h)**	**4.0 (Fe) 1.2 (Ni)**

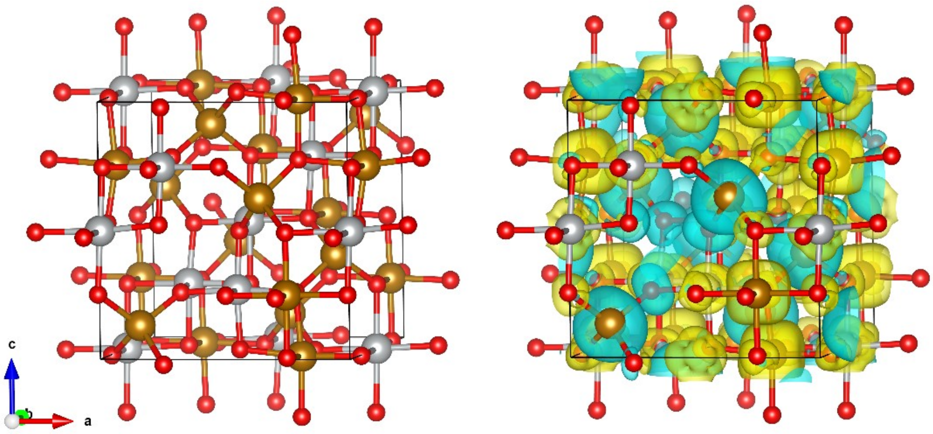

Figure S13. Optimized cell (right) and spin density plot (left) of ferrimagnetic bulk $NiFe_{2-x}O_4$ (x = 0.125) inverse spinel (yellow = spin up, cyan = spin down).

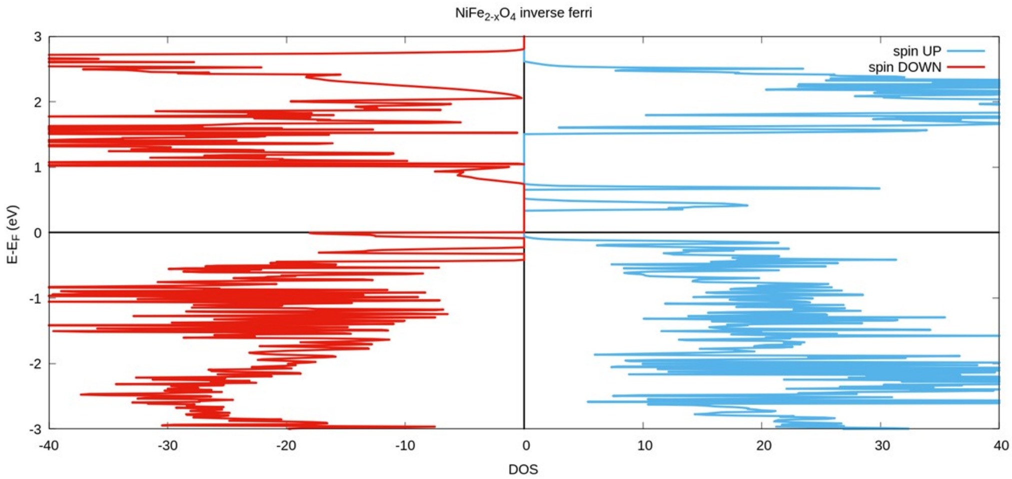

Figure S14. Density of states (DOS) between −3 eV and 3 eV of ferrimagnetic bulk $NiFe_{2-x}O_4$ (x = 0.125) inverse spinel (cyan = spin up, red = spin down).

$ZnFe_2O_4$ ($[Zn_{0.375}Fe_{0.625}]^{A}\{Zn_{0.625}Fe_{1.375}\}^{B}O_4$)

Table S11. Optimized computational data on partially inverse $ZnFe_2O_4$ bulk ($T = 0$ K). The most stable ground state is referred to as 0.00 eV. The experimental lattice parameters are $a = b = c = 8.4437$ Å, as reported in Table S1.

CS (C)	**Magn. Struc. type**	**ΔE (eV)**	**Cell parameters (Å)**	**Cell volume (Å³)**	**Average M–O distance (Å)**	**Abs. Average Mag. Mom. (|μB|)**
Fd-3m	NM	33.18	a=8.17364; b=8.07584; c=7.99209; α=90.15º; β=90.48º; γ=90.70º	527.49	1.81 (Fe-O T_d) 1.94 (Fe-O O_h)	-
	FM	4.15	a=8.46152; b=8.45668; c=8.45897; α=90.10º; β=90.03º; γ=89.94º	605.29	1.91 (Fe-O T_d) 2.04 (Fe-O O_h)	4.1 (Fe)
	AFM	1.46	a=8.42173; b=8.43019; c=8.42671; α=89.97º; β=90.05º; γ=89.96º	598.27	1.90 (Fe-O T_d) 2.04 (Fe-O O_h)	4.0 (Fe)
	Ferri	**0.00**	**a=8.41588; b=8.41537; c=8.41910; α=90.06º; β=90.04º; γ=90.02º**	**596.26**	**1.89 (Fe-O T_d) 2.04 (Fe-O O_h)**	**4.0 (Fe)**

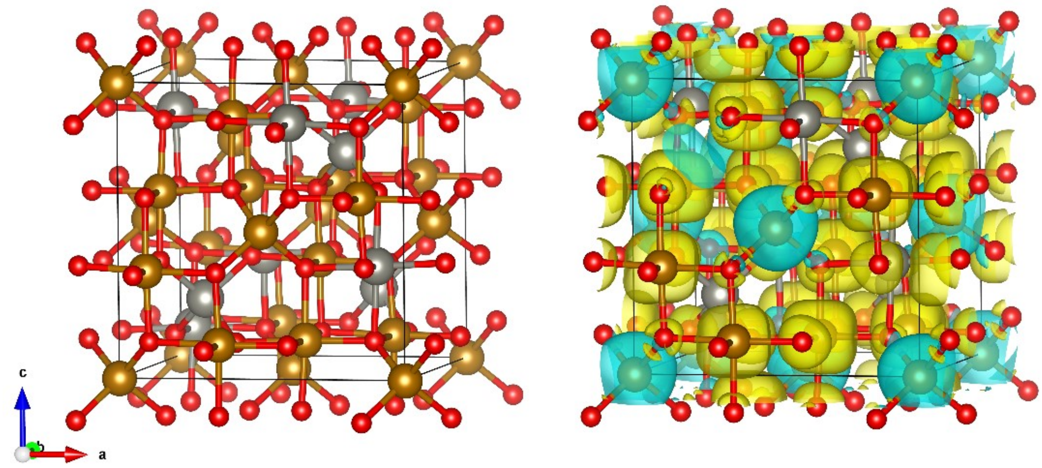

Figure S15. Optimized cell (right) and spin density plot (left) of ferrimagnetic bulk $ZnFe_2O_4$ partially inverse spinel (yellow = spin up, cyan = spin down).

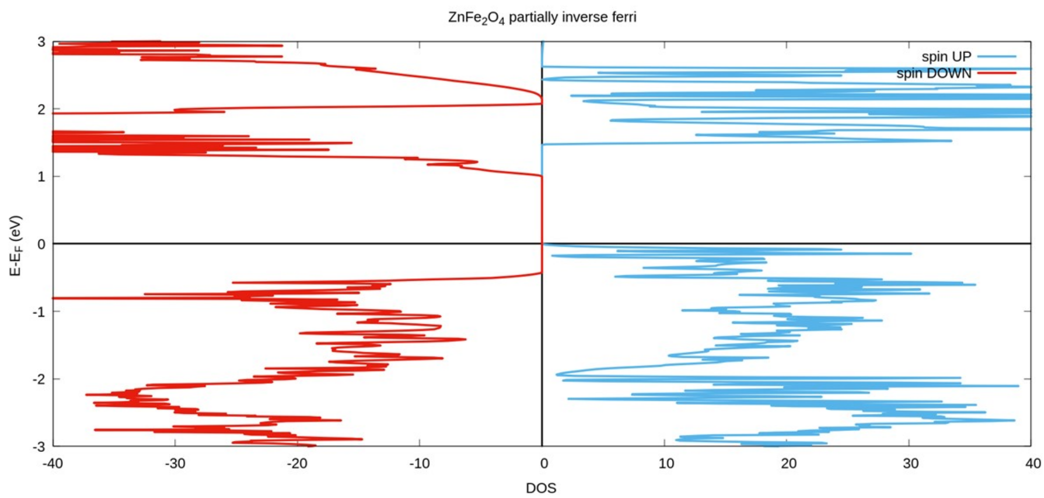

Figure S16. Density of states (DOS) between −3 eV and 3 eV of ferrimagnetic bulk $ZnFe_2O_4$ partially inverse spinel.

$Zn_{0.2}Mn_{0.2}Ni_{0.2}Co_{0.2}Fe_{2.2}O_4$ ($[M_{0.125}Fe_{0.875}]^{A}\{M_{0.750}Fe_{1.250}\}^{B}O_4$)

Two models are built based also on the high-resolution XPS data shown in Figure 4 of the main text.

Table S12. Optimized computational data on partially inverse $Zn_{0.2}Mn_{0.2}Ni_{0.2}Co_{0.2}Fe_{2.2}O_4$ bulk (T = 0 K). The most stable ground state is referred to as 0.00 eV. Some authors reported that the inclusion of Zn^{2+} and Ni^{2+} is difficult in this type of spinel.[38] This was considered for the building of the computational models. The experimental lattice parameters are a=b=c=8.3832 Å as reported in Table S1.

Model a: $[Zn_{0.125}Fe_{0.875}]^{A}\{M_{0.750}Fe_{1.250}\}^{B}O_4$ (M= Co ,Ni, Mn)

CS (C)	Magn. Struc. type	ΔE (eV)	Cell parameters (Å)	Cell volume (Å³)	Average M–O distance (Å)	Abs. Average Mag. Mom. (|μ_B|)
Fd-3m	NM	42.51	a=8.03986; b=7.98983; c=7.91408; α=89.63º; β=89.04º; γ=89.63º	508.29	1.95 (Mn-O O_h) 1.83 (Fe-O T_d) 1.93 (Fe-O O_h) 1.91 (Co-O O_h) 1.95 (Ni-O O_h)	-
	FM	No convergence				
	AFM	Not possible				
	Ferri	**0.00**	**a=8.39186; b=8.41341; c=8.39763; α=90.04º; β=90.38º; γ=90.16º**	**592.87**	**2.11 (Mn-O O_h) 1.89 (Fe-O T_d) 2.03 (Fe-O O_h) 2.07 (Co-O O_h) 2.06 (Ni-O O_h)**	**4.5 (Mn) 4.0 (Fe) 2.6 (Co) 1.6 (Ni)**

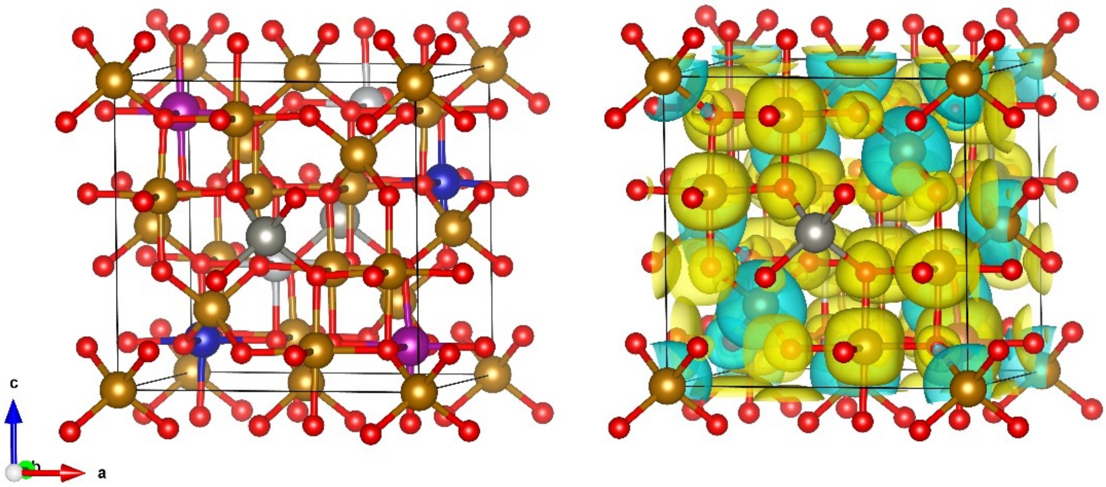

Figure S17. Optimized cell (right) and spin density plot (left) of model a ferrimagnetic bulk $Zn_{0.2}Mn_{0.2}Ni_{0.2}Co_{0.2}Fe_{2.2}O_4$ partially inverse spinel (yellow = spin up, cyan = spin down).

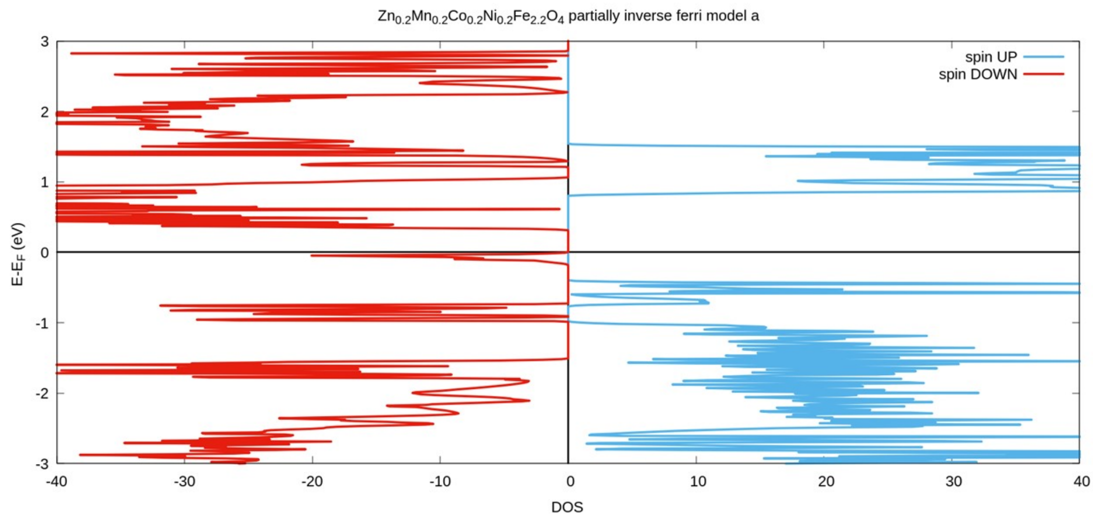

Figure S18. Density of states (DOS) between −3 eV and 3 eV of <u>model a</u> ferrimagnetic bulk $Zn_{0.2}Mn_{0.2}Ni_{0.2}Co_{0.2}Fe_{2.2}O_4$ partially inverse spinel.

Model b: $[Co_{0.125}Fe_{0.875}]^{A}\{M_{0.750}Fe_{1.250}\}^{B}O_4$ (M = Co ,Ni, Mn, Zn)

Table S13. Optimized computational data on partially inverse $Zn_{0.2}Mn_{0.2}Ni_{0.2}Co_{0.2}Fe_{2.2}O_4$ bulk (T = 0 K). The most stable ground state is referred to as 0.00 eV.

CS (C)	**Magn. Struc. type**	**Δ*E* (eV)**	**Cell parameters (Å)**	**Cell vol. (Å^3)**	**Average M–O distance (Å)**	**Abs. Average Mag. Mom. (|μ_B|)**

Fd-3m	NM	43.37	a=7.87034; b=8.09461;
			c=7.96987;
			α=90.21°; β=89.35°; γ=89.40°
				507.67	1.94 (Mn-O O_h)
					1.83 (Fe-O T_d)
					1.92 (Fe-O O_h)
					1.86 (Co-O T_d)
					1.92 (Co-O O_h)
					1.94 (Ni-O O_h)
						-

	FM	No convergence				
	AFM	Not possible				

	Ferri 1	0.29	a=8.40296; b=8.41844;
			c=8.40276;
			α=90.26°; β=90.48°; γ=89.91°
				594.38	2.12 (Mn-O O_h)
					1.89 (Fe-O T_d)
					2.04 (Fe-O O_h)
					1.97 (Co-O T_d)
					2.08 (Co-O O_h)
					2.06 (Ni-O O_h)
						4.5 (Mn)
						4.0 (Fe)
						2.6 (Co)
						1.6 (Ni)

	Ferri 2	**0.00**	**a=8.39750; b=8.41351;** **c=8.39746;** **α=90.26°; β=90.48°; γ=89.91°**	**593.27**	**2.12 (Mn-O O_h)** **1.89 (Fe-O T_d)** **2.06 (Fe-O O_h)** **1.95 (Co-O T_d)** **2.08 (Co-O O_h)** **2.06 (Ni-O O_h)**	**4.5 (Mn)** **4.0 (Fe)** **2.6 (Co)** **1.6 (Ni)**

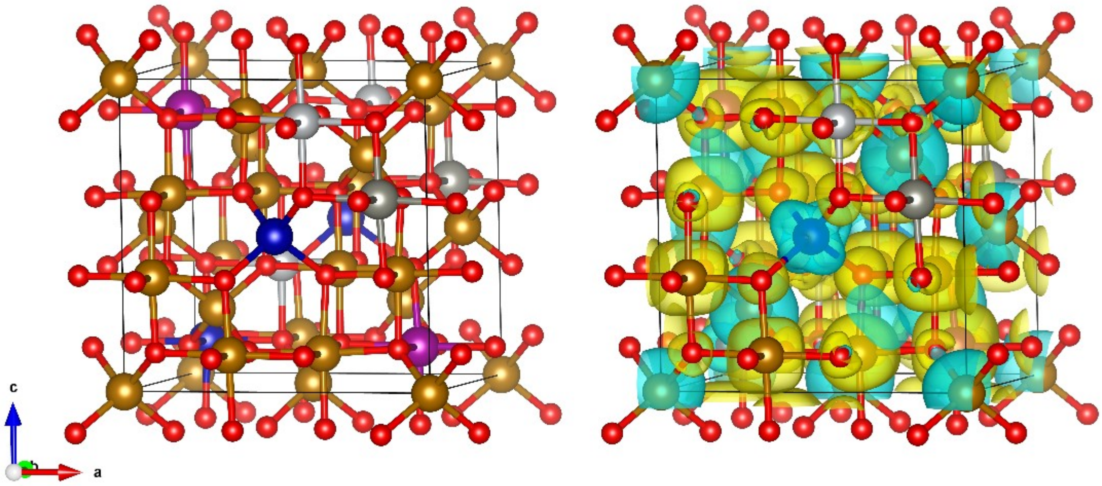

Figure S19. Optimized supercell (right) and spin density plot (left) of model b ferrimagnetic bulk $Zn_{0.2}Mn_{0.2}Ni_{0.2}Co_{0.2}Fe_{2.2}O_4$ partially inverse spinel (yellow = spin up, cyan = spin down).

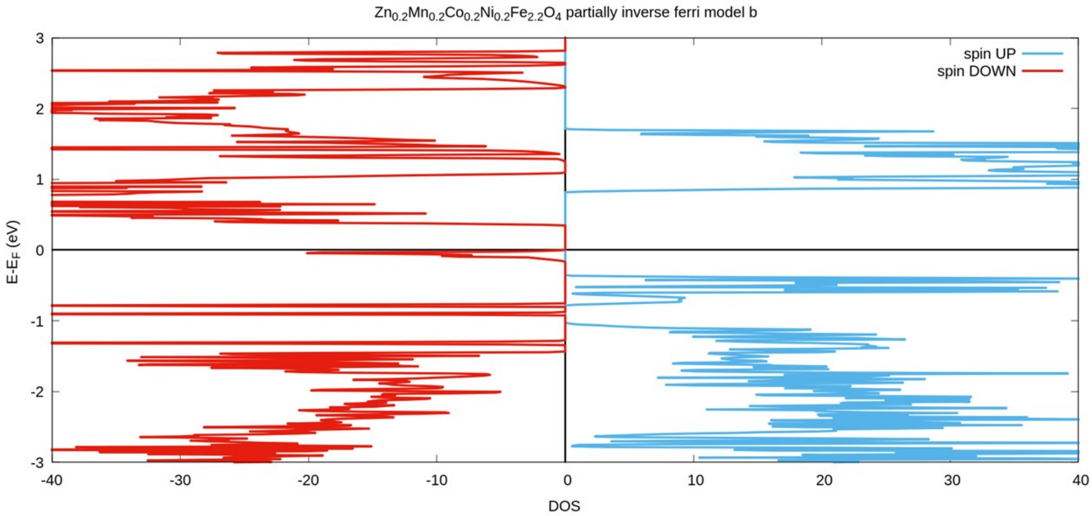

Figure S20. Density of states (DOS) between −3 eV and 3 eV of <u>model b</u> ferrimagnetic bulk $Zn_{0.2}Mn_{0.2}Ni_{0.2}Co_{0.2}Fe_{2.2}O_4$ partially inverse spinel.

Table S14. Calculated minimum band gaps for the spinels under study (E_g in eV). NR = data not been reported in literature.

System	Calc. minimum band gaps (E_g, eV) (this work)	Exp. band gaps (E_g, eV) (this work)	Reported calculated band gaps (E_g, eV)
$NiFe_2O_4$ (inverse)	1.55 (spin ↑)/ 1.14 (spin ↓)	1.58	1.56 (spin↓)/ 2.26 (spin ↑) inverse spinel (mBJLDA potential);[39] 1.6 (spin↓) / 1.9 (spin ↑) (LSDA+U, U for Fe/Ni= 4.5/4.0 eV);[40] 1.10 (GGA+U, U= 3 eV);[41] 2.2 (spin↓)/ 1.6 (spin ↑) inv. spinel (PBE+U, U_{Ni}=6 eV, U_{Fe}=4.5eV)[42]
$NiFe_{2-x}O_4$ (x= 0.125) (inverse)	0.37 (spin ↑)/ 0.73 (spin ↓)	1.58	N.R.
$CoFe_2O_4$ (partially Inverse)	0.66 (spin ↑)/ 0.49 (spin ↓)	1.48	0.63 (LMTO+LSDA+U, U=4eV);[43] 1.8 (spin ↑)/ 0.9 (spin ↓) (LSDA+U, U Fe/Co=4.5/4.0 eV);[44] 0.09 $(Co)_{Td}(Fe_2)_{Oh}O_4$ (normal spinel);[45] 0.08, 0.00 for two possible Co ions distribution of $(Co_{0.75}Fe_{0.25})_{Td}(Co_{0.25}Fe_{1.75})_{Oh}O_4$;[45] 0.16, 0.24, 0.00 for three possible Co ions distribution of $(Co_{0.5}Fe_{0.5})_{Td}(Co_{0.5}Fe_{1.5})_{Oh}O_4$;[45] 0.30, 0.00, 0.00 for three possible Co ions distribution of $(Co_{0.25}Fe_{0.75})_{Td}(Co_{0.75}Fe_{1.25})_{Oh}O_4$;[45] 0.72 $(Fe)_{Td}(CoFe)_{Oh}O_4$ (inv. spinel)[45] (PBE+U+J, for Fe U=4.22 and J=0.80 eV and for Co U=4.08 and J=0.79 eV)[45]
$ZnFe_2O_4$ (partially Inverse)	1.46 (spin ↑)/ 1.42 (spin ↓)	1.70	3.21 normal spinel (B3LYP);[46] 4.06 normal spinel (PBE0);[46] 3.31 normal spinel (PBE0);[47] 2.21 normal spinel (PBE+U, U= 5.25 eV);[47] 2.89 normal spinel (PBE+U/eV/cvGW/BSE, U=1eV);[48] 3.83 normal spinel (PBE+U/ eV/cvGW/BSE, U=3eV)[48]
$Zn_{0.2}Mn_{0.2}Ni_{0.2}Co_{0.2}Fe_{2.2}O_4$ (partially Inverse)	Model a : 1.19 (spin ↑)/ 0.30 (spin ↓) Model b : 1.16 (spin ↑)/ 0.34 (spin ↓)	1.51	NR

REFERENCES

[1] D. Lim, H. Kong, N. Kim, C. Lim, W.-S. Ahn and S.-H. Baeck, *ChemNanoMat* **2019**, *5*, 1296–1302.

[2] A. Z. Alhakemy, A. M. Elseman, M. G. Fayed, A. B. Ahmed Amine Nassr, A. El-Hady Kashyout and Z. Wen, *Ceram. Int.* **2022**, *48*, 5442–5449.

[3] K. Lankauf, K. Cysewska, J. Karczewski, A. Mielewczyk-Gryń, K. Górnicka, G. Cempura, M. Chen, P. Jasiński and S. Molin, *Int. J. Hydrogen Energy* **2020**, *45*, 14867–14879.

[4] G. Liu, K. Wang, X. Gao, D. He and J. Li, *Electrochim. Acta* **2016**, *211*, 871–878.

[5] C. Simon, J. Timm, D. Tetzlaff, J. Jungmann, U.-P. Apfel and R. Marschall, *ChemElectroChem* **2021**, *8*, 227–239.

[6] Y. Hu, X. Zhao, F. Li, Q. Dong, B. Wen, D. Sun, W. Liang and X. Lyu, *ACS Appl. Energy Mater.* **2023**, *6*, 9985–9993.

[7] Y.-Q. Zhang, M. Li, B. Hua, Y. Wang, Y.-F. Sun and J.-L. Luo, *Appl. Catal., B* **2018**, *236*, 413–419.

[8] L. S. Ferreira, T. R. Silva, V. D. Silva, R. A. Raimundo, T. A. Simões, F. J. A. Loureiro, D. P. Fagg, M. A. Morales and D. A. Macedo, *Adv. Powder Technol.* **2022**, *33*, 103391.

[9] C. Si, Y. Zhang, C. Zhang, H. Gao, W. Ma, L. Lv and Z. Zhang, *Electrochim. Acta* **2017**, *245*, 829–838.

[10] S. Jha, P. Jain, R. Palkovits and P. Popinand Ingole, *J. Mater. Chem. A* **2023**, *11*, 23034-23047.

[11] N. M. Malima, M. D. Khan, J. Choi, R. K. Gupta and N. Revaprasadu, *Mater. Chem. Phys* **2023**, *302*, 127770.

[12] S. B. Sundararaj and S. Thangavelu, *J. Phys. Chem. C* **2023**, *127*, 4953–4966.

[13] J.-B. Tan, P. Sahoo, J.-W. Wang, Y.-W. Hu, Z.-M. Zhang and T.-B. Lu, *Inorg. Chem. Front.* **2018**, *5*, 310–318.

[14] J. Zander, J. P. Wölfel, M. Weiss, Y. Jiang, N. Cheng, S. Zhang and R. Marschall, *Adv. Funct. Mater.* **2023**, *34*, 2310179.

[15] J. Baek, M. D. Hossain, P. Mukherjee, J. H. Lee, K. T. Winther, J. Leem, Y. Jiang, W. C. Chueh, M. Bajdich and X. L. Zheng, *Nat. Commun.* **2023**, *14*, 5936.

[16] Y. Zhang, T. Lu, Y. Ye, W. Dai, Y. a. Zhu and Y. Pan, *ACS Appl. Mater. Interfaces* **2020**, *12*, 32548–32555.

[17] Y. Zhang, W. Dai, P. Zhang, T. Lu and Y. Pan, *J. Alloys Compd.* **2021**, *868*, 159064.

[18] A. Martinez-Lazaro, A. Caprì, I. Gatto, J. Ledesma-García, N. Rey-Raap, A. Arenillas, F. I. Espinosa-Lagunes, V. Baglio and L. G. Arriaga, *J. Power Sources* **2023**, *556*, 232417.

[19] S. Campagna Zignani, M. Lo Faro, S. Trocino and A. S. Aricò, *Energies* **2020**, *13*, 1720.
[20] A. Caprì, I. Gatto, C. Lo Vecchio, S. Trocino, A. Carbone and V. Baglio, *ChemElectroChem* **2023**, *10*, e202201056.
[21] A. Carbone, S. C. Zignani, I. Gatto, S. Trocino and A. S. Aricò, *Int. J. Hydrog. Energy* **2020**, *45*, 9285–9292.
[22] T. Pandiarajan, L. John Berchmans and S. Ravichandran, *RSC Adv.* **2015**, *5*, 34100–34108.
[23] J. Lee, H. Jung, Y. S. Park, S. Woo, N. Kwon, Y. Xing, S. H. Oh, S. M. Choi, J. W. Han and B. Lim, *Chem. Eng. J.* **2021**, *420*, 127670.
[24] A. Caprì, I. Gatto, C. Lo Vecchio and V. Baglio, *Chem. Mater.* **2023**, *1*, 553-562.
[25] C. Busacca, S. C. Zignani, A. Di Blasi, O. Di Blasi, M. Lo Faro, V. Antonucci and A. S. Aricò, *Int. J. Hydrog. Energy* **2019**, *44*, 20987–20996.
[26] A. Y. Faid, A. O. Barnett, F. Seland and S. Sunde, *Int. J. Hydrog. Energy* **2022**, *47*, 23483–23497.
[27] a) P. Giannozzi, O. Baseggio, P. Bonfà, D. Brunato, R. Car, I. Carnimeo, C. Cavazzoni, S. de Gironcoli, P. Delugas, F. Ferrari Ruffino, A. Ferretti, N. Marzari, I. Timrov, A. Urru and S. Baroni, *J. Chem. Phys.* **2020**, *152*, 154105; b) P. Giannozzi, O. Andreussi, T. Brumme, O. Bunau, M. Buongiorno Nardelli, M. Calandra, R. Car, C. Cavazzoni, D. Ceresoli, M. Cococcioni, N. Colonna, I. Carnimeo, A. Dal Corso, S. de Gironcoli, P. Delugas, R. A. DiStasio, A. Ferretti, A. Floris, G. Fratesi, G. Fugallo, R. Gebauer, U. Gerstmann, F. Giustino, T. Gorni, J. Jia, M. Kawamura, H. Y. Ko, A. Kokalj, E. Küçükbenli, M. Lazzeri, M. Marsili, N. Marzari, F. Mauri, N. L. Nguyen, H. V. Nguyen, A. Otero-de-la-Roza, L. Paulatto, S. Poncé, D. Rocca, R. Sabatini, B. Santra, M. Schlipf, A. P. Seitsonen, A. Smogunov, I. Timrov, T. Thonhauser, P. Umari, N. Vast, X. Wu and S. Baroni, *J. Condens. Matter Phys.* **2017**, *29*, 465901; c) P. Giannozzi, S. Baroni, N. Bonini, M. Calandra, R. Car, C. Cavazzoni, D. Ceresoli, G. L. Chiarotti, M. Cococcioni and I. Dabo, *J. Condens. Matter Phys.* **2009**, *21*, 395502.
[28] a) M. Cococcioni and S. De Gironcoli, *Phys. Rev. B* **2005**, *71*, 035105; b) B. Himmetoglu, R. M. Wentzcovitch, M. Cococcioni, *Phys. Rev. B* **2011**, *84*, 115108; c) S. L. Dudarev, G. A. Botton, S. Y. Savrasov, C. J. Humphreys, A. P. Sutton, , *Phys. Rev. B* **1998**, *57*, 1505-1509.
[29] J. Klimeš, D. R. Bowler and A. Michaelides, *J. Condens. Matter Phys.* **2009**, *22*, 022201.
[30] K. Laasonen, A. Pasquarello, R. Car, C. Lee and D. Vanderbilt, *Phys. Rev. B* **1993**, *47*, 10142.
[31] A. Dal Corso, *Comput. Mater. Sci.* **2014**, *95*, 337–350.
[32] H. J. Monkhorst and J. D. Pack, *Phys. Rev. B* **1976**, *13*, 5188.
[33] N. Marzari, D. Vanderbilt, A. De Vita and M. Payne, *Phys. Rev. Lett.* **1999**, *82*, 3296.

[34] a) S. Mugiraneza and A. M. Hallas, *Commun. Phys.* **2022**, *5*, 95; b) S. Blundell, *Magnetism in condensed matter*, OUP Oxford, **2001**.; c) *Magnetism and transition metal complexes*, Courier Corporation, **2008**.

[35] K. Momma and F. Izumi, *J. Appl. Crystallogr.* **2011**, *44*, 1272–1276.

[36] T. Williams and C. Kelley in *gnuplot 5.4. An interactive plotting program. Version 5.4. December, 2020*, *Vol.* **2021**.

[37] J. Klein, L. Kampermann, B. Mockenhaupt, M. Behrens, J. Strunk and G. Bacher, *Adv. Funct. Mater.* **2023**, *33*, 2304523.

[38] F. Arteaga-Cardona, U. Pal, J. M. Alonso, P. de la Presa, M.-E. Mendoza-Alvarez, U. Salazar-Kuri and M. A. Mendez-Rojas, *J. Magn. Magn.* **2019**, *490*, 165496.

[39] M. Meinert and G. Reiss, *J. Condens. Matter Phys.* **2014**, *26*, 115503.

[40] Q.-C. Sun, H. Sims, D. Mazumdar, J. Ma, B. Holinsworth, K. O'Neal, G. Kim, W. Butler, A. Gupta and J. Musfeldt, *Phys. Rev. B* **2012**, *86*, 205106.

[41] L. Idrissi, N. Tahiri, O. El Bounagui and H. Ez-Zahraouy, *J. Supercond. Nov. Magn.* **2020**, *33*, 1369–1375.

[42] J. Wangchhuk and S. R. Meher, *Phys. Lett., A* **2022**, *443*, 128202.

[43] V. Antonov, B. Harmon and A. Yaresko, *Phys. Rev. B* **2003**, *67*, 024417.

[44] B. Holinsworth, D. Mazumdar, H. Sims, Q.-C. Sun, M. Yurtisigi, S. Sarker, A. Gupta, W. Butler and J. Musfeldt, *Appl. Phys. Lett.* **2013**, *103*.

[45] Y. Hou, Y. Zhao, Z. Liu, H. Yu, X. Zhong, W. Qiu, D. Zeng and L. Wen, *J. Phys. D* **2010**, *43*, 445003.

[46] A. de Rezende, M. de Oliveira, R. Ribeiro, W. Mesquita, J. d. J. Marques, N. d. S. Magalhaes, J. Lemes, E. Longo and M. d. C. Gurgel, *Mater.* **2022**, *25*, e20220219.

[47] D. Fritsch, *J. Condens. Matter Phys.* **2018**, *30*, 095502.

[48] A. C. Ulpe and T. Bredow, *ChemPhysChem* **2020**, *21*, 546–551.